Collimated thermal radiation transfer via half Maxwell's fish-eye lens for thermophotovoltaics

Haejun Chung, Zhiguang Zhou, and Peter Bermel

Citation: Appl. Phys. Lett. **110**, 201111 (2017); doi: 10.1063/1.4983679
View online: http://dx.doi.org/10.1063/1.4983679
View Table of Contents: http://aip.scitation.org/toc/apl/110/20
Published by the American Institute of Physics

Collimated thermal radiation transfer via half Maxwell's fish-eye lens for thermophotovoltaics

Haejun Chung, Zhiguang Zhou, and Peter Bermel[a)]
Birck Nanotechnology Center, Purdue University, 1205 W. State St., West Lafayette, Indiana 47907, USA

(Received 14 December 2016; accepted 5 May 2017; published online 19 May 2017)

Thermophotovoltaics (TPV) convert heat into electricity by capturing thermal radiation with a photovoltaic (PV) cell, ideally at efficiencies of 50% or more. However, excess heating of the PV cell from close proximity to the emitter substantially reduces the system efficiency. In this work, we theoretically develop and numerically demonstrate an approach to fundamentally improving TPV systems that allow for a much greater separation of an emitter and a receiver. Thus, we solve the excess heating dilemma, required for achieving theoretically high efficiencies. It consists of a spherically graded index lens known as Maxwell's Fish-Eye (MFE) structure, capable of collimating hemispherical emission into a much narrower range of angles, close to the normal direction. To fully characterize the power radiation profile of the MFE, we perform finite-difference time-domain simulations for a quarter MFE and then map it onto a Gaussian beam approximation. The modeled beam properties are subsequently used to study a half MFE. In an optimized half MFE design, 90% of all thermal photons reach a receiver at a distance of 100 λ; by comparison, only 15.6% of a blackbody emitter reach a receiver in the same geometry. It is also shown that the emission achieved by a half MFE can lead to a photon recycling rate above 95% for below bandgap photons at an emitter-receiver separation of 100 λ. By applying a half MFE, the absolute TPV efficiency can be improved from 5.74% to 37.15%, which represents a significant step forward in realizing high-efficiency TPV systems. *Published by AIP Publishing.* [http://dx.doi.org/10.1063/1.4983679]

Thermophotovoltaic (TPV) systems convert heat into electricity by thermal radiation of photons onto a low-bandgap photovoltaic (PV) diode.[1,2] In principle, the efficiency of TPV systems can be 50% or more.[3,4] Nonetheless, there are many sources of loss, which include sub-bandgap photons, carrier thermalization, and optical losses. As a result, many studies have focused on suppressing subbandgap photon emission of an emitter with concepts such as magnetic-polariton-enhancement,[5] photonic crystal resonances,[4,6–9] and rare earth atomic transitions.[10,11] To further suppress sub-bandgap losses, a process known as photon recycling has been proposed, in which a filter is added to the system[12] so that sub-bandgap photons can be reflected back for re-absorption by the emitter. Success in photon recycling depends on a high view factor, which is defined as the fraction of thermally emitted photons that reach the receiver. Thus, when photon recycling is included, the efficiency of a TPV system is more sensitive to any decrease in its view factor.[4,13] In either case, the PV diode should always be placed close to a non-directional thermal emitter. The selective thermal emitter flux at high temperatures can be much more intense than unconcentrated sunlight, which can also rapidly heat the PV diode. Drawbacks to this heating include substantial reductions in efficiency, reliability, and safety. In a typical TPV setup, an emitter is placed under vacuum to prevent any convective and conductive thermal loss, while a cold side PV diode is also placed within the vacuum to secure a high view factor. To address this issue, most experimental TPV work uses active water cooling which consumes energy to cool the PV diode,[10,14,15] as shown in Fig. 1(a), possibly canceling out some or all of the benefits of the energy generated. As the gap between the emitter and the PV diode increases, the view factor and efficiency decrease significantly. This is the reason why most TPV experiments use large emitters and receivers separated by a relatively small distance.

In this work, we develop an approach to fundamentally improve TPV systems that allow for a much greater separation between an emitter and an receiver so that it maintains theoretically high efficiencies while avoiding difficult trade-offs to maintain the cold side performance of the system. In particular, we numerically present half Maxwell's fish-eye (MFE) lens to redirect standard blackbody radiation following Lambert's cosine law into a narrow, directed emission cone. This directed emission can help to greatly decrease the dependence of efficiency on the separation between the emitter and the receiver. This performance thus allows for the separation to be increased greatly so that the cold side can be removed from vacuum, as shown in Fig. 1(b). This allows for the ready implementation of improved passive cooling approaches in air. At the same time, it also allows one to use a less selective emitter that may be more thermally stable, given the improved photon recycling. Compared with approaches such as 2D photonic crystal super-collimation,[16] which extend the focal point slightly farther at specific wavelengths, the present approach allows for high-temperature operations across a broad bandwidth.

We will now summarize our method to calculate the view factor and the resulting TPV efficiency. We use 2-D Finite Difference Time Domain (FDTD) simulations[17] to validate a directed emission and photon recycling effect of the half MFE. Since the thermal radiation process includes different intensities at different emission angles, which is challenging to directly simulate, most TPV simulations

[a)]Electronic mail: pbermel@purdue.edu

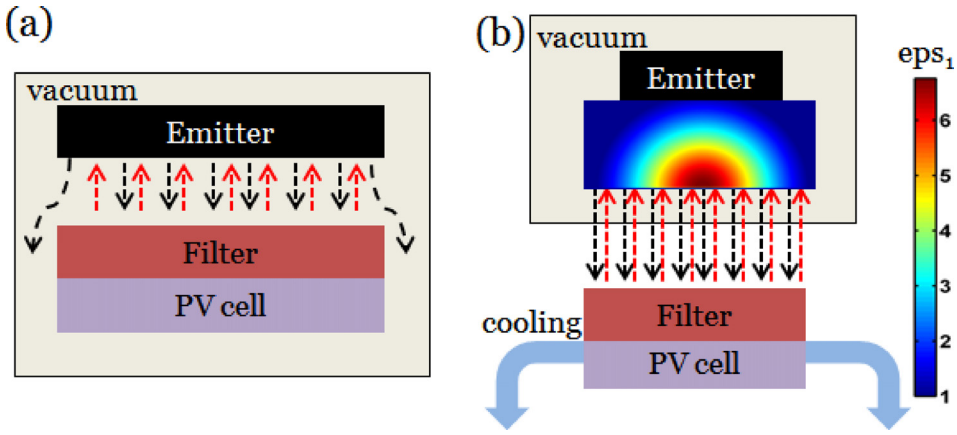

FIG. 1. Two alternatives for thermo-photovoltaic power generation: (a) a conventional TPV system, which requires placing all components under high vacuum; (b) the alternative TPV system proposed in this work, consisting of half Maxwell's fish-eye (MFE) structure collimating thermal emission for the far field. The rainbow colors in the MFE represent the range of values for the real part of the dielectric constant for the half MFE. Here, the cold side PV diode can be removed from vacuum because of highly collimated thermal radiation.

assume Kirchoff's law of thermal radiation and are performed with a plane-wave source starting from the cold side.[11,18,19] Alternatively, one can directly calculate thermal radiation in FDTD with uncorrelated white noise generated at each pixel of a thermal source.[20,21] In this work, to reproduce Lambert's Cosine law associated with blackbody radiation, a line of dipole currents is assigned to the boundary of the half MFE and the emitter in FDTD. This approach is chosen to properly capture the dispersion of wave propagation in free space. As shown in Fig. 2(d), the simulated incident source follows the Cosine law radiation pattern in a free space. In our simulations, the view factor is computed by $F(\lambda) = 1 - P_{sideloss}/P_{emit}(\lambda)$, where $P_{sideloss}$ is the electromagnetic flux which does not reach the PV diode and absorbed by perfectly match layers and $P_{emit}(\lambda)$ is an emitted flux from the half MFE. The detailed TPV efficiency calculation has been developed and validated in previous work.[11] The only modification to the established procedure here is to replace emittance with an effective emittance $\epsilon_{eff}(\lambda)$, given by

$$\epsilon_{eff}(\lambda) = \epsilon(\lambda) \times F(\lambda), \tag{1}$$

where $\epsilon(\lambda)$ is the emittance spectrum and F is the view factor obtained in this work.

The MFE structure used in this work has been studied for perfect imaging,[22] directed emission,[23] coupler design,[24] and antenna design.[25] It has a spherical graded refractive index function $n(r)$, given by

$$n(r) = \frac{n_c}{1 + \left(\frac{r}{R}\right)^2}, \tag{2}$$

where n_c is a constant, R is the radius of the MFE, and r is the radial distance from the center. An initial emission profile at the half MFE surface can be described as two separate beams,[26] but it is not clear how two separate beams can propagate and form a far-field radiation pattern. To characterize the half MFE beam properties, we first simulate quarter Maxwell's fish-eye structure in 2-D FDTD, as shown in Fig. 2.

As shown in Fig. 2(a), the simulated H_z field profile for the quarter MFE is used to define both the waist size (w_0) and the focal length of the half MFE. Then, the Gaussian beam approximation[27,28] is directly applied to generate an intensity distribution of the beam, as shown in Fig. 2(b). The analytic Gaussian beam expression approximates the beam intensity profile as well as the spot size $w(z)$ which is related to the full width at half maximum (FWHM) by $w(z) = \mathrm{FWHM}/(2\ln 2)$.

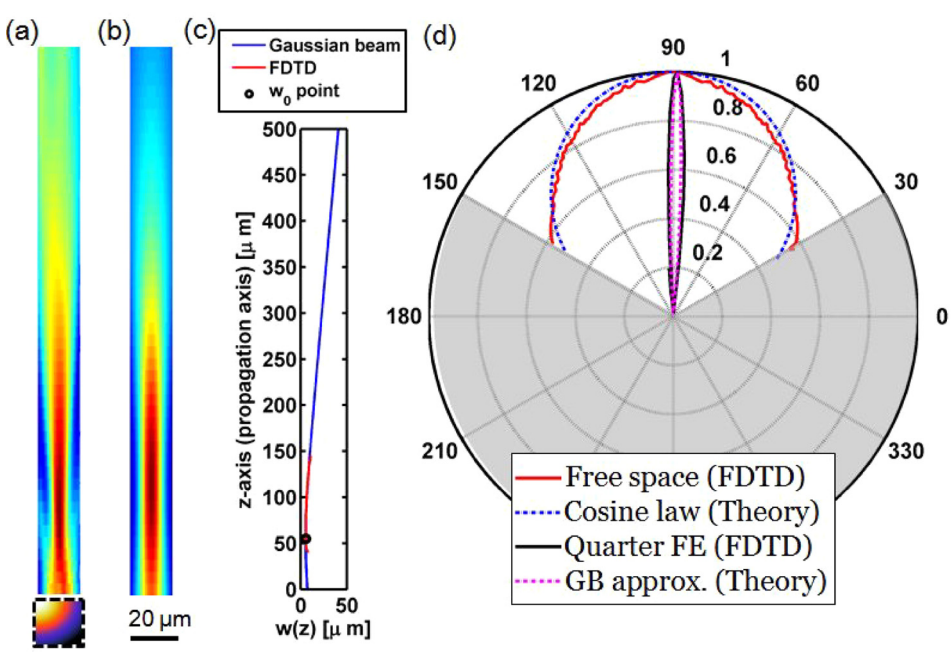

FIG. 2. Power radiation profile for quarter Maxwell's fish-eye structure: (a) magnetic field (Hz) profile, as calculated by FDTD. The dashed box in the bottom shows the refractive index profile of the structure. (b) Magnetic field (Hz) profile of Gaussian Beam approximation with a focal length of 60 μm. (c) Spot size versus propagation length in the Gaussian Beam approximation and the FDTD. (d) Far-field radiation pattern calculated analytically and by FDTD simulations.

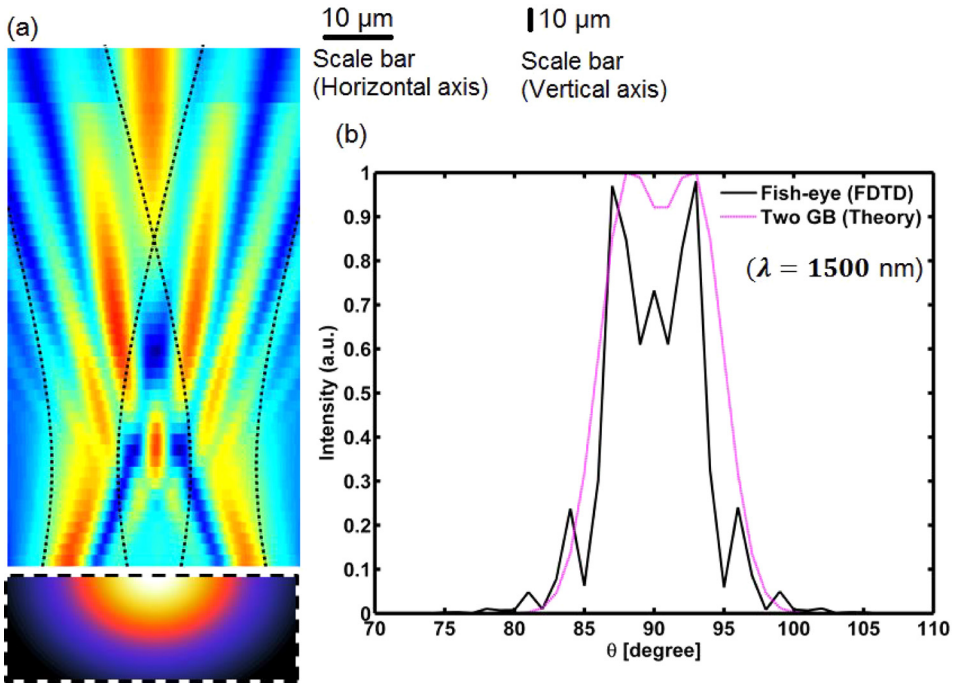

FIG. 3. Power radiation profiles for half Maxwell's fish-eye: (a) magnetic field H_z profile of this simulation. The dashed lines represent the spot sizes of two split Gaussian beams. To show a clear emission profile, the aspect ratio is not to scale. The dashed box indicates the refractive index profile of the structure. (b) Far-field collimated radiation intensity as a function of angle at a distance of 150 μm. The exact FDTD simulation results show a close match to two superimposed Gaussian beams.

Figure 2(c) shows the spot size versus propagation length for the Gaussian beam approximation, compared to FDTD. They agree very well within the simulated distance. Thus, to predict the ultra-far field pattern for the quarter MFE, the Gaussian Beam Approximation can be used directly, without requiring a relatively expensive full-wave computation. Figure 2(d) presents the far-field emission pattern for the quarter MFE in the Gaussian Beam Approximation. The quarter MFE emission is limited to a narrow range of angles, which shows that it can redirect Lambert's law hemispherical radiation pattern into a highly directed radiation pattern.

Now, we simulate a half MFE emission pattern over a distance of 250 μm from the emitter. As shown in Fig. 3, the two beams on the surface of the half MFE are observed as predicted, but there is also a non-negligible amount of emission between the two beams at the center of the half MFE surface. As a result, as shown in Fig. 3(a), the two peaks of the emission are not clearly maintained. However, as shown in Fig. 3(b), the majority of emitted power is still maintained within the spot size of the two split Gaussian beams for 150 μm propagation, which implies that further simulations can be substituted by two split Gaussian Beams after a sufficient propagation distance.

The half MFE was designed for the ray-optics regime, where the feature size is relatively larger than the operating wavelength. However, the MFE has a continuous variation in the refractive index; thus, an "ideal" fish-eye should have negligible feature sizes. To resolve this paradox, in this work, we study the operating limit of the half MFE for various MFE radii in 2D FDTD simulations. The maximum refractive index is set to 2.6 at the center, while the grid spacing is set to 50 nm for both axes. The theoretical view factor for this simulation setup (distance, 142.5 μm; receiver width, 45 μm) is 15.6%. As shown in Fig. 4, 18 μm radius half MFE achieves a relatively higher view factor, which implies that it operates in the ray-optics regime, while a smaller radius half MFE has a relatively low view factor. These results imply that it can be used as a low-loss, free-space light collimator with a certain cutoff frequency. In other words, it provides directed emission at the desired frequencies, whereas undesired frequency components are scattered, preventing sub-bandgap absorption by the PV diode.

Finally, we consider the benefits of placing a chirped filter on top of the PV diode for sub-bandgap photon recycling. In the simulation setup described in Fig. 5(a), all the emission reaching the perfectly matched layer is considered as a loss, while light passing through the filter is considered to be absorbed by the receiver; only the light returning to the half MFE is considered to be re-absorbed by the emitter. As shown in Fig. 5(b), the chirped filter used in this study has a minimum resolution of 50 nm; thus, it does not have an ideal cutoff at the bandgap of the PV diode. Figure 5(c) shows the

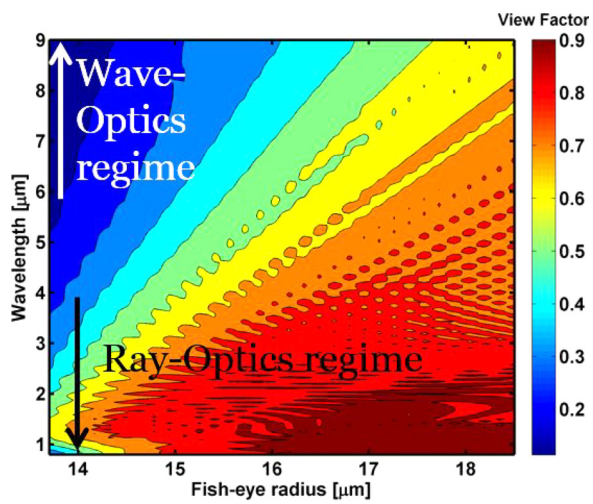

FIG. 4. Contour plot showing view factor versus half MFE radius r and wavelength λ. When $r \gg \lambda$, the half MFE behaves as if it was in the ray-optics regime and collimates light. On the other hand, when $r \sim \lambda$, the device behaves as if it was in the wave-optics regime and does not collimate effectively. This regime crossover phenomenon helps to minimize excess heating of a distant receiver.

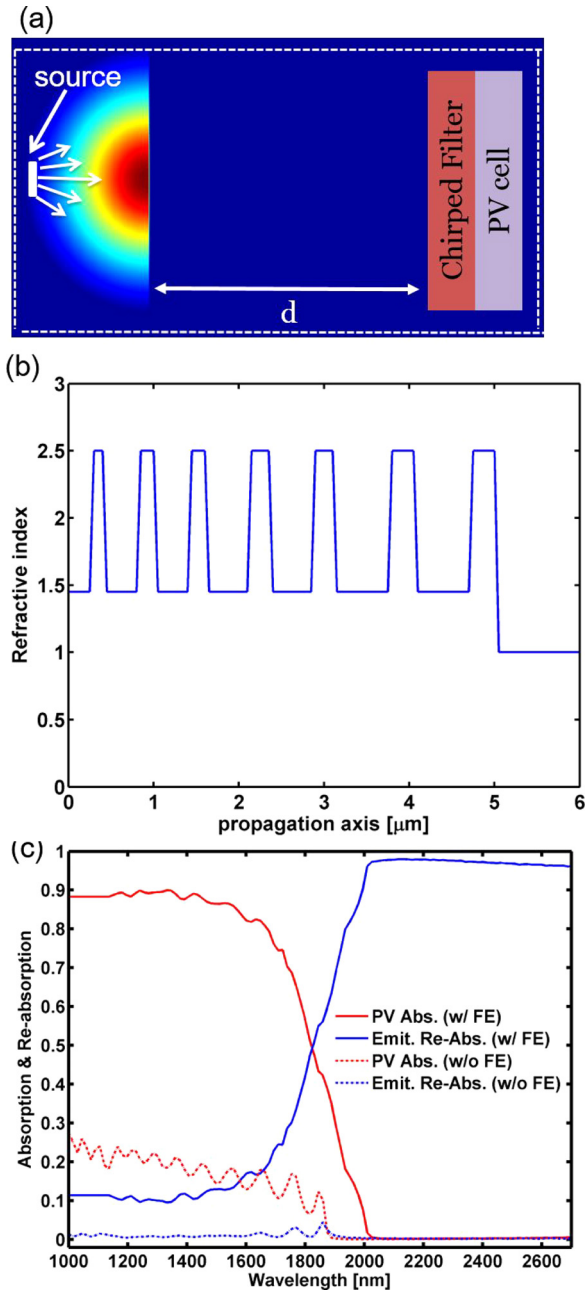

FIG. 5. (a) 2-D FDTD simulation geometry representing the proposed thermophotovoltaic system; (b) chirped filter refractive index versus depth to achieve above photon recycling; and (c) 2-D FDTD result showing the PV absorption and emitter re-absorption spectrum for an emitter-receiver separation of 100 λ.

simulated absorption and reabsorption profiles. The absorption reaches almost 90% for the above bandgap photons, while 95% of sub-bandgap photons are reabsorbed by the emitter. A 10% recycling rate for the above bandgap photons results from the non-ideal filter design, which does not fully account for the range of angles reaching it. The resulting TPV heat-to-electricity conversion efficiency is 37.15% at 1573 K; by comparison, the bare blackbody emitter only reaches 5.74% under the same conditions. To further extend the emitter-receiver separation, two split Gaussian beam approach can be directly used to calculate the radial field intensity profile along the propagation.

In conclusion, we have numerically demonstrated collimated thermal radiation transfer across long distances using the half MFE. To properly describe the half MFE beam characteristics, a quarter MFE was first simulated and modeled in the Gaussian Beam Approximation. It has been shown that its emission pattern follows the Gaussian beam pattern, while the half MFE emission is more complex. However, a majority of emitted power in the half MFE still remains within the spot radius of the two Gaussian beams. The modeled beam properties are then used to study the half MFE beam properties. With an optimal radius, a view factor of 90% is achieved across an emitter-receiver separation of 100 λ; by comparison, a bare emitter would only have had a view factor of 15.6%. In addition, it has been shown that the directed emission achieved by the half MFE can result in over a 95% photon recycling rate for below bandgap photons at 100 λ separation. Allowing for very large separations between thermal emitters and receivers without penalty represents a significant step forward in realizing several important applications. One strong example is the ultimate passively cooled TPV system, in which one can take advantage of all fundamental cooling mechanisms (conductive, convective, and radiative) in parallel, to increase TPV heat-to-electricity conversion efficiencies from 5.74% to 37.15%.

The authors thank Enas Sakr for valuable discussions. Support was provided by the Department of Energy, under DOE Cooperative Agreement No. DE-EE0004946 (PVMI Bay Area PV Consortium) and the National Science Foundation, under Award No. EEC1454315-CAREER: Thermophotonics for Efficient Harvesting of Waste Heat as Electricity.

[1]D. Chubb, *Fundamentals of Thermophotovoltaic Energy Conversion* (Elsevier, 2007).
[2]T. Bauer, *Thermophotovoltaics: Basic Principles and Critical Aspects of System Design* (Springer Science & Business Media, 2011).
[3]N.-P. Harder and P. Würfel, Semicond. Sci. Technol. **18**, S151 (2003).
[4]P. Bermel, M. Ghebrebrhan, W. Chan, Y. X. Yeng, M. Araghchini, R. Hamam, C. H. Marton, K. F. Jensen, M. Soljačić, J. D. Joannopoulos, S. G. Johnson, and I. Celanovic, Opt. Express **18**, A314 (2010).
[5]L. Wang and Z. Zhang, Appl. Phys. Lett. **100**, 063902 (2012).
[6]D. Woolf, J. Hensley, J. Cederberg, D. Bethke, A. Grine, and E. Shaner, Appl. Phys. Lett. **105**, 081110 (2014).
[7]J. B. Chou, Y. X. Yeng, A. Lenert, V. Rinnerbauer, I. Celanovic, M. Soljačić, E. N. Wang, and S.-G. Kim, Opt. Express **22**, A144 (2014).
[8]E. Rephaeli and S. Fan, Opt. Express **17**, 15145 (2009).
[9]I. Celanovic, N. Jovanovic, and J. Kassakian, Appl. Phys. Lett. **92**, 193101 (2008).
[10]B. Bitnar, W. Durisch, and R. Holzner, Appl. Energy **105**, 430 (2013).
[11]E. Sakr, Z. Zhou, and P. Bermel, Appl. Phys. Lett. **105**, 111107 (2014).
[12]T. Xiao, G. Scranton, V. Ganapati, J. Holzrichter, P. Peterson, and E. Yablonovitch, in *CLEO: Applications and Technology* (Optical Society of America, 2016), p. ATu1K–2.
[13]Z. Zhou, E. Sakr, Y. Sun, and P. Bermel, Nanophotonics **5**, 1 (2016).
[14]A. Datas and C. Algora, Prog. Photovoltaics: Res. Appl. **21**, 1040 (2013).
[15]A. Lenert, D. M. Bierman, Y. Nam, W. R. Chan, I. Celanović, M. Soljačić, and E. N. Wang, Nat. Nanotechnol. **9**, 126 (2014).
[16]P. T. Rakich, M. S. Dahlem, S. Tandon, M. Ibanescu, M. Soljačić, G. S. Petrich, J. D. Joannopoulos, L. A. Kolodziejski, and E. P. Ippen, Nat. Mater. **5**, 93 (2006).
[17]S. Hagness and A. Taflove, *Computational Electrodynamics: The Finite-Difference Time-Domain Method* (Artech House, Norwood, MA, 2000).
[18]K. A. Arpin, M. D. Losego, A. N. Cloud, H. Ning, J. Mallek, N. P. Sergeant, L. Zhu, Z. Yu, B. Kalanyan, G. N. Parsons, G. S. Girolami, J. R. Abelson, S. Fan, and P. V. Braun, Nat. Commun. **4**, 2630 (2013).
[19]P. Bermel, M. Ghebrebrhan, M. Harradon, Y. X. Yeng, I. Celanovic, J. D. Joannopoulos, and M. Soljacic, Nanoscale Res. Lett. **6**, 549 (2011).
[20]C. Luo, A. Narayanaswamy, G. Chen, and J. Joannopoulos, Phys. Rev. Lett. **93**, 213905 (2004).

[21]A. W. Rodriguez, O. Ilic, P. Bermel, I. Celanovic, J. D. Joannopoulos, M. Soljačić, and S. G. Johnson, Phys. Rev. Lett. **107**, 114302 (2011).
[22]R. Merlin, J. Opt. **13**, 024017 (2011).
[23]A. Dhouibi, S. N. Burokur, A. de Lustrac, and A. Priou, Appl. Phys. Lett. **102**, 024102 (2013).
[24]H. Kurt, B. Oner, M. Turduev, and I. Giden, Opt. Express **20**, 22018 (2012).
[25]A. Ourir, A. de Lustrac, and J.-M. Lourtioz, Appl. Phys. Lett. **88**, 084103 (2006).
[26]F. Sun, X. C. Ge, and S. He, Prog. Electromagn. Res. **110**, 313 (2010).
[27]G. A. Deschamps, Electron. Lett. **7**, 684 (1971).
[28]H. Kogelnik, Appl. Opt. **4**, 1562 (1965).